Nano Research

Open Access

Research Article

Space-confined vapor deposited molecular ferroelectric film for photovoltaic devices

Chen Wang[1,2], Shan Cong[2] ✉, Lingbo Xiao[3], Chao-ran Huang[2], Ruonan Wang[2], Ruijie Li[2], Lutao Li[2], Guifu Zou[4] ✉, and Qiang Zhang[1] ✉

[1] College of Mechanical and Electronic Engineering, Shandong University of Science and Technology, Qingdao 266590, China
[2] College of Energy, Soochow Institute for Energy and Materials Innovations, and Key Laboratory of Advanced Carbon Materials and Wearable Energy Technologies of Jiangsu Province, Soochow University, Suzhou 215000, China
[3] Department of Applied Physics, Zhejiang University of Science and Technology, Hangzhou 310023, China
[4] School of Advanced Energy, Sun Yat-sen University, Shenzhen 518107, China

Cite this article: *Nano Research*, **2025**, *18*, 94907221. https://doi.org/10.26599/NR.2025.94907221

ABSTRACT: Molecular ferroelectrics, characterized by outstanding photoelectric and unique ferroelectric properties, invigorate the field of ferroelectric photovoltaics. Nonetheless, the performance of molecular ferroelectric devices is hindered by fine grains resulting from poor high-temperature stability. In this work, we successfully achieved micron-grained molecular ferroelectric films by using the space-confined vapor deposited method. The optimized film exhibited a significant increase in grain size from the nanometer level (0.08 μm) to the micrometer level (~ 2 μm), leading to improved optoelectronic and ferroelectricity. Furthermore, it optimizes the energy level and enhances the photovoltaic performance of vertical devices. Research on the mechanism shows that high annealing temperature and inhibiting component loss play an important role in obtaining large grain films. This work provides new research ideas for improving the quality of molecular ferroelectric films and provides valuable reference for the fabrication of high performance molecular ferroelectric photovoltaic devices.

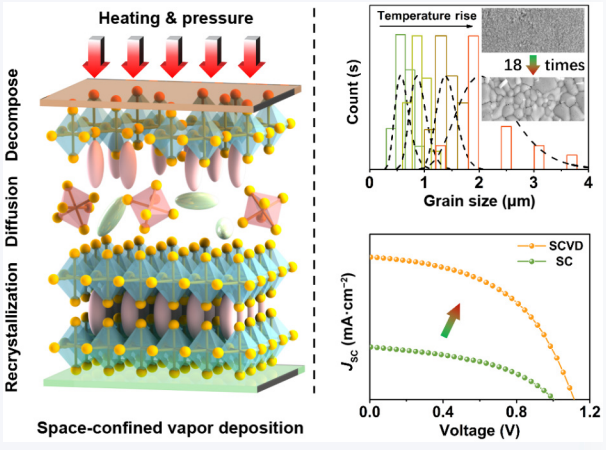

KEYWORDS: molecular ferroelectric, large grain, space confinement, photovoltaic devices

1 Introduction

Ferroelectric materials with polarization fields that promote carrier separation and transport hold great potential for photovoltaic devices [1–7]. Currently, researches on the ferroelectric photovoltaic devices primarily focus on single-crystal materials [8, 9]. This preference stems from the fact that large domains in single crystal materials are beneficial to promote carrier separation and transport [10, 11]. For easy-to-prepare, cost-effective polycrystalline materials, the defects at grain boundaries leads to the formation of domain walls, restricting the domains size and weakening the ferroelectric response [12]. Consequently, increasing the grain size of polycrystalline films has been demonstrated as an effective approach to enhance the ferroelectric device performances [13].

Molecular ferroelectrics exhibit distinctive ferroelectricity, including high Curie temperature, strong remnant polarization, multiple polar axes, and excellent optoelectronic properties such as narrow bandgap, high absorption coefficient and efficient photoluminescence, which make them highly promising for potential photovoltaic applications [14–17]. Xiao et al. achieved passivation of interface defects, optimization of energy level structure, and improvement of device performance by *in-situ* growth of molecular ferroelectrics on the surface of the light-absorbing layer [18]. By incorporating molecular ferroelectrics into the active layer, Xu et al. and Zhang et al. effectively enhance the built-in electric field within the photovoltaic device, resulting in an increase in open-circuit voltage (V_{OC}) [19, 20]. By using ferroelectricity to promote carrier transport in the multiple

Received: November 26, 2024; **Revised:** December 23, 2024
Accepted: December 25, 2024

✉Address correspondence to Shan Cong, congshan1352@suda.edu.cn; Guifu Zou, zougf3@mail.sysu.edu.cn; Qiang Zhang, zhangqiangskd@sdust.edu.cn

quantum well electronic structure, solar cells based on molecular ferroelectric achieve the highest V_{OC} among n = 1 two-dimensional Ruddlesden–Popper perovskite solar cells [15]. However, the inferior quality of the films, especially the small domains resulting from fine grains, degrades the ferroelectricity of polycrystalline films and limits the device performance [21]. High-temperature annealing has proven to be an effective method for controlling the grain size of inorganic ferroelectrics [22, 23]. Nevertheless, achieving large-grain films in molecular ferroelectrics becomes challenging due to their poor high-temperature stability (Fig. 1(a)).

In this work, micron-grained molecular ferroelectric films are successfully obtained using space-confined vapor deposition (SCVD) technology. A significant increase in grain size is observed by SCVD at a temperature above the decomposition point. The SCVD process also led to notable enhancements in the optoelectronic and ferroelectric properties, including reduced band gaps, decreased density of defect states, enhanced carrier mobility, optimized energy level structures, and strong ferroelectric properties. Additionally, the SCVD-processed device (SCVD-device) exhibits excellent photovoltaic performance, further enhancing the performance of two-dimensional (2D) (n = 1) ferroelectric photovoltaic devices.

2 Results and discussion

To achieve high photovoltaic performance, molecular ferroelectric (4,4-difluoropiperidinium)$_2$PbI$_4$ is selected as the active layer, exhibiting unique ferroelectric properties such as a multipolar axis, a high Curie temperature (428.5 K), and high spontaneous polarization (10 μC/cm^2), along with excellent optoelectronic properties, including a high absorbance coefficient (~ 10^5 cm^{-1}), narrow band gap (2.24 eV), and low processing temperature (100 °C) [24]. Details of the experiments related to material synthesis and film preparation are provided in the Electronic Supplementary Material (ESM). The SCVD process involves two transparent conductive substrates spin-coated with precursor (fluorine-doped tin oxide/film (abbreviated as film 1) and indium tin oxide/film (abbreviated as film 2)) and held together under mechanical pressure (Fig. S1 in the ESM). The upper plate is kept at a specified temperature (such as 300 °C), and the initial temperature of the bottom plate is room temperature. Continuous mechanical pressure builds space confinement between films to reduce material loss at high temperatures. During the SCVD process, the film 1 decomposes at high temperature and deposited downward to assist the crystallization of film 2 (Fig. 1(b)). The top-view scanning electron microscopy (SEM) images in Fig. 1(c) show that the grain size significantly increases after SCVD, producing a continuous and dense film without defects such as pinholes. Compared with spin coating film (SC-film), the average grain size of SCVD processed film (SCVD-film) increases from the nanometer level to the micrometer level. The transmission electron microscope image reveals a polar space group *Aba*2 (point group *mm*2) with a 2.23 Å interplanar spacing corresponding to the (004) orientation, indicating strong in-plane orientation aligned with the corner-sharing inorganic octahedral framework (Fig. 1(d))

The SCVD process is characterized to elucidate the film

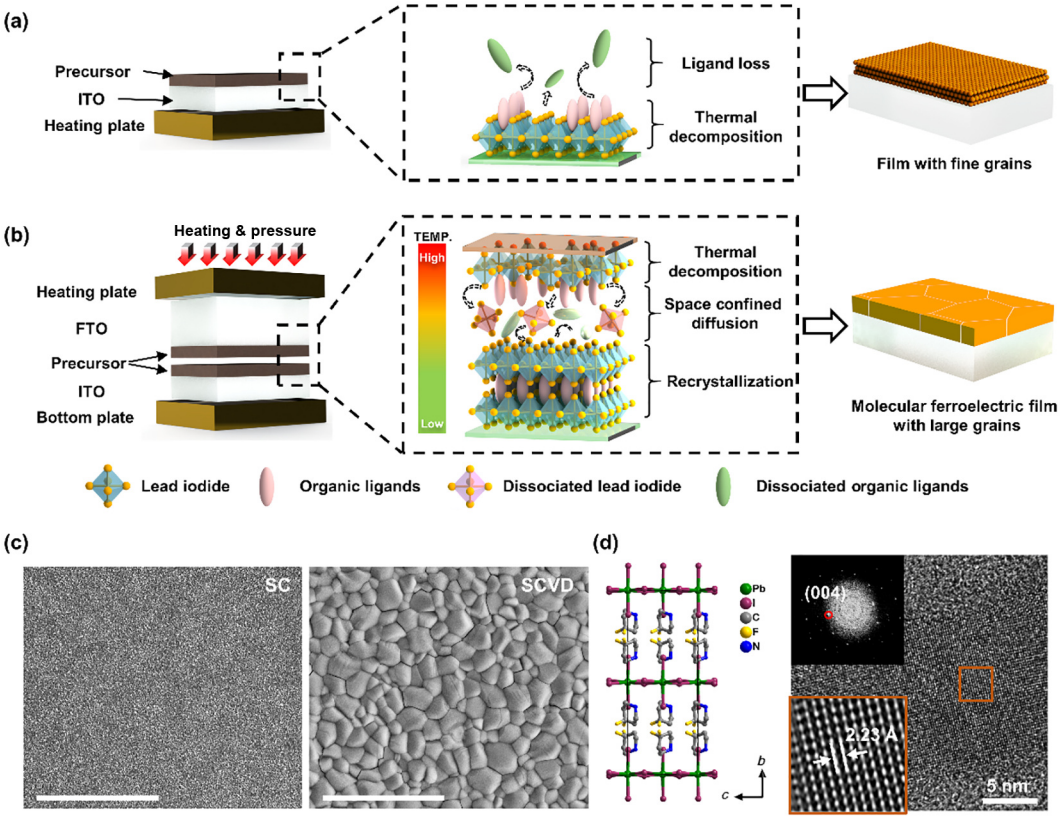

Figure 1 The SCVD process. (a) Illustration of the SC (spin coating) process. (b) Illustration of the SCVD process. (c) The top-view SEM images and grain size statistics of molecular ferroelectric film obtained by SC and SCVD (scale bar: 5 μm). (d) Ball stick model of (4,4-difluoropiperidinium)$_2$PbI$_4$ and the transmission electron microscope image, the upper left image is the fast Fourier transform processed image of the orange region, and the lower left image is the inverse fast Fourier transform processed image of the orange region.

optimization mechanism. SEM images of SCVD films at different annealing condition indicate that grain size varies with temperature and duration (Figs. S2 and S3 in the ESM). The bottom plate temperature can appropriately reflect the annealing environment of the film. As the annealing time increases, the bottom plate temperature increases rapidly and stabilizes, and the stabilization temperature increases with the upper plate temperature (Fig. S4 in the ESM). As the bottom plate temperature increased from 80 to 160 °C, the average grain size grew from 0.61 to 2.23 μm, representing an increase by two orders of magnitude compared to the SC-films (0.08 μm, Fig. 2(a)). However, at 160 °C, the presence of large grains (3–4 μm) led to poor continuity and the introduction of impurities (Fig. S5 in the ESM). Appropriate annealing temperature and duration are critical for obtaining dense, continuous, and large-grain molecular ferroelectric films. To investigate the film temperature during the SCVD process, finite element calculations are conducted. The physical model and parameter settings can be found in Fig. S6 in the ESM. The steady-state heat distribution in Fig. 2(b) shows that the final stable temperature of the film exceeds 200 °C when the upper plate temperature is set at 300 °C. The transient heat distribution results reveal that the temperature transferees rapidly from film 1 to film 2, and the film temperature increases rapidly and stabilizes above 200 °C (Fig. 2(c) and Video S1 in the ESM). Thermogravimetric analysis indicates the decomposition and loss of organic ligands occurs at 200 °C (Fig. 2(d)), and the temperature of the molecular ferroelectric during the SCVD process is higher than the decomposition temperature. To uncover the decomposition of materials, X-ray diffractometer (XRD) analysis is performed (Fig. 2(e)). The XRD of the SCVD-film 1 displayed decomposition product PbI_2 (12.8°) and other impurity peaks (9.9° and 11.4°), while the peak intensity of the SCVD-film 2 increased without any impurity peaks appears. The Fourier transform infrared (FTIR) reveals weaker C–F bonds in film 1 compared to film 2, indicating partial decomposition of SCVD-film 1 (Fig. 2(f)). In order to evaluate the effect of film 1, the XRD and FTIR results of film 1 with different concentrations are characterized. XRD peaks before SCVD correspond to the (020) and (040) orientations of molecular ferroelectrics, indicating crystallization at room temperature (Fig. S7(a) in the ESM), but with poor crystallinity and significant background. Without precursor spin-coating on film 1 (0 M), SCVD enhanced film 2 peaks, with new peaks at 9.9° and 12.8° corresponding to decomposition product (Fig. S7(b) in the ESM). As the concentration of film 1 increases, the 9.9° peak in film 2 is suppressed at 0.4 M (Fig. S7(c) in the ESM), and at 0.8 M, impurity peaks disappear (Fig. S7(d) in the ESM), suggesting high concentrations of film 1 inhibit decomposition of film 2. Moreover, under the condition of film 1 (0.8 M), strong molecular ferroelectric characteristic peaks are still detected in film 2 after the SCVD process, even without precursor (0 M) for film 2 (Fig. S7(e) in the ESM). The top-view SEM image show incomplete quadrilateral nanosheets in film 2, consistent with the orthogonal point group of the low-temperature phase (Fig. S8 in the ESM), Energy dispersive X-ray spectroscopy revealed the distribution of C, Pb and I elements, consistent with molecular ferroelectric elements (Fig. S9 in the ESM). FTIR is used to characterize the C–F vibration in the

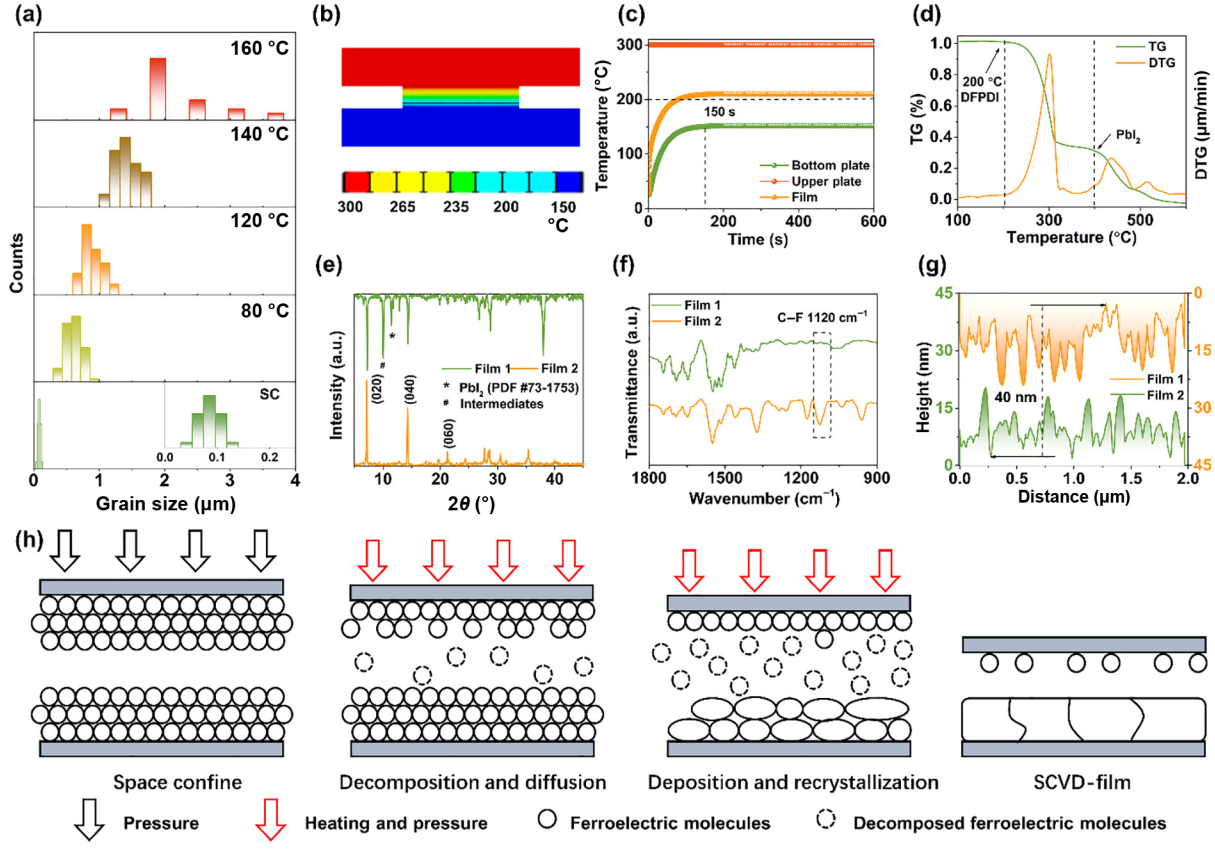

Figure 2 Characterization of SCVD process. (a) Grain size statistics, (b) steady state thermal analysis calculation results, (c) transient thermal analysis calculation results; (d) thermogravimetry analysis results, (e) XRD results of film 1 (0.8 M) and film 2 (0.8 M) after SCVD, (f) FTIR results of film 1 (0.8 M) and film 2 (0.8 M) after SCVD, (g) the corresponding height distribution from atomic force microscope results, and (h) the schematic diagram of the SCVD process.

molecular ferroelectric structure. There is always a C–F vibration peak at 1120 cm^{-1} in film 2 (Fig. S10(a) in the ESM), not obvious in film 1 (Fig. S10(b) in the ESM), which might due to the decomposition at high temperatures. Figure S10(c) in the ESM reveals the optical photos of film 1 before and after SCVD. Film 1 (0.4 M) decomposes after SCVD, whereas a higher concentration of film 1 (0.8 M) helps prevent complete decomposition, thereby maintaining film continuity. These results indicate that film 1 decomposes during the SCVD process, diffuses and recrystallizes on film 2. To characterize the space confinement during SCVD processing, atomic force microscope is employed to characterize the surface roughness. The roughness of film 1 and film 2 before SCVD are 5.62 and 3.14 nm, respectively (Fig. S11 in the ESM). The cross-sectional curves show that the distance between the two films is only 40 nm, sufficient to maintain space confinement (Fig. 2(g)). Based on the aforementioned results, we propose the following hypothesis: During the SCVD process, the film 1 decomposes at high temperature, and the space confinement effect ensures that the decomposition products diffuse to the film 2. The decomposition and diffusion of film 1 can simultaneously inhibit the decomposition of film 2, achieve high-temperature sintering, and obtain molecular ferroelectric films with large grain sizes (Fig. 2(h)). It is worth noting that too high a temperature may still cause the loss of film 2, which may be because the excessive decomposition of film 1 makes it difficult to inhibit the decomposition of film 2.

The increased grain size significantly impacts the optoelectronic and ferroelectric properties. The X-ray photoelectron spectroscopy (XPS) results are uncovered in Fig. S12 in the ESM. The XPS spectra of C 1s, N 1s, F 1s, I 3d, and Pb 4f after SCVD treatment show noticeable changes. Using the C–C binding energy (284.8 eV) for calibration, the integrated area of the N 1s peak increased from 3304.4 to 9722.0, indicating surface enrichment of organic ligands on the SCVD-film (Table S1 in the ESM). A more pronounced change is observed in the F 1s, where the integrated area increased from 6461.2 to 34,777.8 after SCVD treatment. The similar changes occur in the I 3d (Fig. 3(a)), which are deconvoluted into two distinct oxidation states: I^- at 618.8 and 630.3 eV, and triiodide (I_3^-) at 620.1 and 631.7 eV [25]. After SCVD, the I_3^-/I^- area ratio increases substantially from 0.11 and 0.07 to 0.43 and 0.30, respectively, suggesting an enrichment of I on the film surface, consistent with the observed changes in N and F. In contrast, the Pb 4f peak area ratio remains relatively unchanged, with a slight increase in the Pb oxide peak area, which is attributed to the inevitable oxidation during SCVD. The survey results reveal that the films contain all the elements. In addition to surface characterization, SCVD also affects the optoelectronic properties. The ultraviolet–visible (UV–Vis) spectra in Fig. 3(b) reveal that the absorbance of the film after SCVD is increased, and the band gap reduced from 2.31 to 2.24 eV. Narrow bandgap could improve light utilization and is more conducive to the application of optoelectronic devices. Photoluminescence peaks also red-shift from 526 to 546 nm in SCVD-film (Fig. 3(c)), with additional UV–Vis and photoluminescence data under various annealing conditions provided in Fig. S13 in the ESM. Ultraviolet photoelectron spectroscopy reveals that SCVD-film shifts the $E_{cut\text{-}off}$ from 17.20 to 17.25 eV, and $E_v - E_f$ decreases from 0.87 to 1.52 eV (Fig. S14 in the ESM). Figure 3(d) is a schematic diagram of the calculated energy level structure of SC-film and SCVD-film. The SC-film has high valence band and conduction band, indicating p-type properties. The valence band and conduction band of the SCVD-film are low and the Fermi level is close to the conduction band, showing an n-type property. This may be related to the surface termination: the accumulation of organic ligands on the surface of SCVD-films regulates the surface energy levels [26, 27]. The change in energy level is also characterized through kelvin probe force microscope. The surface potential of SCVD-films increased compared to SC-film (Fig. 3(e)). As the annealing temperature increases from 160 to 300 °C, the surface potential changes from −0.508 to −0.439 eV (Fig. S15 in the ESM). In addition, space charge limited current is carried out to characterize the defect state concentration and electron mobility of the film (Fig. 3(f)). The defect density of molecular ferroelectric films can be examined by following equation [20],

$$N_{defects} = 2\varepsilon\varepsilon_0 V_{TFL}/eL^2 \quad (1)$$

where e is the elementary charge, L is the thickness of the molecular ferroelectric film, ε is the relative dielectric constant of the molecular ferroelectric film, ε_0 is the vacuum dielectric constant, and V_{TFL} is the trap filling limit voltage. Moreover, the mobility of carriers can be evaluated by the following equation [20],

$$\mu = 8JL^3/9\varepsilon\varepsilon_0 V^2 \quad (2)$$

where J, L, ε, ε_0 and V respectively represent the current density, molecular ferroelectric film thickness, relative dielectric constant, vacuum dielectric constant and applied voltage. The trap state density of the SC-treated film is 6.9×10^7 cm^{-3}, and the trap state density of the SCVD-treated film is reduced to 2.4×10^7 cm^{-3}. Moreover, the electron mobility of SCVD-processed film increases from 0.35×10^{-5} to 1.25×10^{-5} $cm^2/(V{\cdot}s)$. The ferroelectricity of film is also significantly improved after SCVD. Under external electric field excitation, the SC-film has weak out-of-plane amplitude contrast and small phase change induced by polycrystalline nature, and the domain size is limited by small-sized grains, showing poor ferroelectric response (Fig. 3(g)). The hysteretic dependence of the local piezoresponse force microscopy (PFM) phase and amplitude reveal the coercive field is small and the ferroelectricity is "soft", which may be related to more defects in the film (Fig. 3(h)). As a comparison, the PFM morphology, out-of-plane amplitude and phase diagrams of the SCVD-film in Fig. 3(i) reveal that large-grained films exhibit more pronounced amplitude contrasts, greater phase changes, and a significant increase in domain size. The hysteretic dependence of the PFM phase and amplitude (Fig. 3(j)) suggested a typical ferroelectric polarization switching process with enhanced coercive field, the ferroelectric response becomes "hard", benefiting from the low defect density. In addition, in-plane PFM are performed to assess the impact of SCVD treatment on polarization performance (Fig. S16 in the ESM). The amplitude and phase mapping show clear in-plane signals, aligned with the material's in-plane orientation. After SCVD treatment, the in-plane amplitude response is significantly enhanced, with an expanded phase area and larger domain sizes. To indicate the influence of grain orientation on the hysteresis curves, PFM hysteresis measurements are conducted on multiple grains, and results from six randomly selected locations are shown in Fig. S17 in the ESM. Minor variations in amplitude and phase across different locations are observed, might be induced by grain orientation. However, these variations are minimal compared to the effects induced by SCVD treatment. The SCVD-film demonstrates a more pronounced phase hysteresis, higher amplitude, and larger butterfly

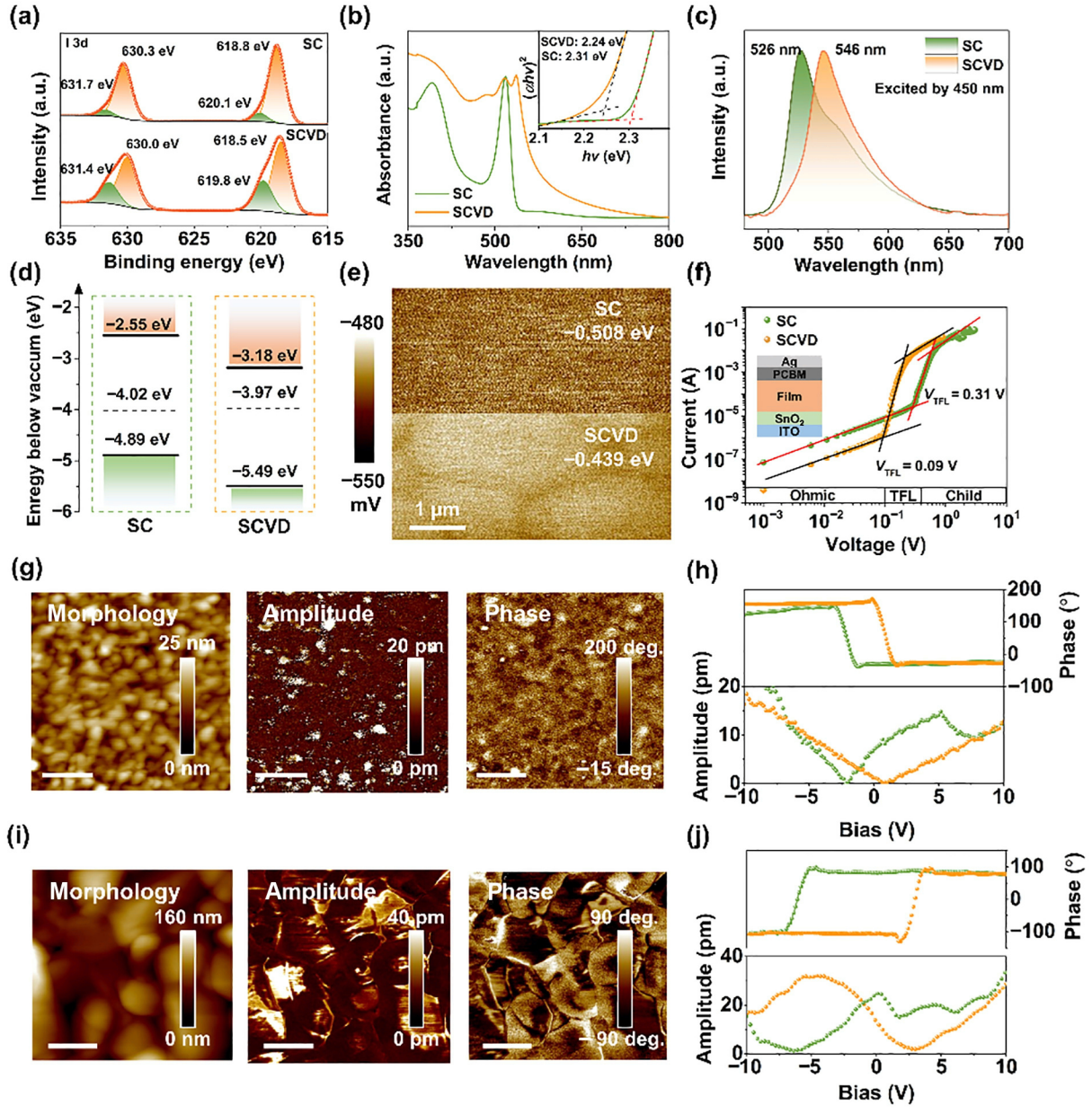

Figure 3 The characterization of SC-film and SCVD-film. (a) XPS spectra of I 3d. (b) UV–Vis spectra and corresponding Tauc plots. (c) Photoluminescence spectra, excited by 450 nm. (d) Energy level structure. (e) Kelvin probe force microscope. (f) Space charge limited current. The PFM results of SC-film: (g) morphology, out-of-plane amplitude, and out-of-plane phase (scale bar: 500 nm) and (h) hysteretic dependence of the phase and amplitude. The PFM results of SCVD-film: (i) morphology, out-of-plane amplitude, and out-of-plane phase (scale bar: 500 nm) and (j) hysteretic dependence of the phase and amplitude.

loops. All in all, SCVD treatment enhances the out-of-plane amplitude signal to levels comparable with the in-plane signals and significantly improves the material's ferroelectric response, which is beneficial for device performance.

Highly efficient ferroelectric solar cells hold significant research value within the photovoltaic devices. Vertical ferroelectric photovoltaic devices (structure: ITO/NiO_X/film/PCBM/BCP/Ag, Fig. 4(a)) are fabricated using molecular ferroelectric (4,4-difluoropiperidinium)$_2PbI_4$ as active layers, and the influence of SCVD on device performance is studied. Additionally, Cross-sectional images of SCVD-devices show large grain size and sharp interfaces, leading to reduced grain boundary density, few interface defects and enhanced charge separation (Fig. 4(b)). The schematic of the energy level structure illustrates that SCVD-device facilitates a well-matched band structure (Fig. 4(c)). Specifically, the low valence band (−5.49 eV) and conduction band (−3.18 eV) are conducive to the effective separation and transportation of photogenerated charges. Besides, the dielectric properties of the film are revealed in the curve of dielectric loss and capacitance performance as a function of frequency (Fig. 4(d)). At frequencies above 10^5 Hz, there is no difference in capacitance and dielectric loss between the two films; however, SCVD-films at medium and low frequencies (below 10^4 Hz) exhibit low capacitance and reduced dielectric loss, potentially due to decreased defects and suppressed space charge polarization [28]. Moreover, electrochemical impedance spectroscopy are conducted to evaluate the capacitive response of devices (Fig. 4(e)).

Nyquist plots indicate that the SCVD-device exhibit larger fitted

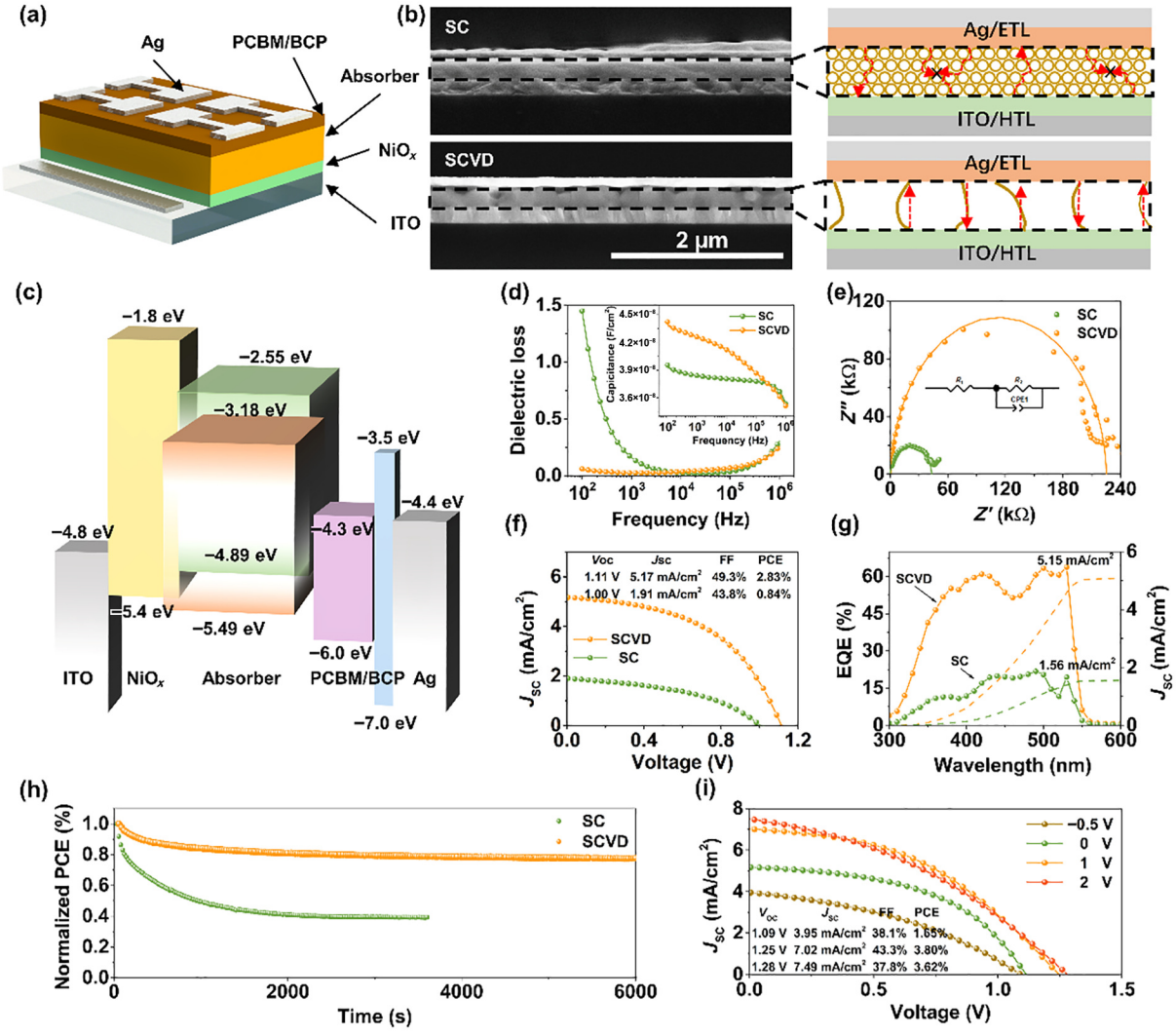

Figure 4 Characterization of vertical photovoltaic devices. (a) Schematic diagram of the device structure; (b) cross-section images of devices and the corresponding schematic diagram; (c) device band structure, green: SC-film, orange: SCVD-film; (d) dielectric loss–frequency curves; (e) electrochemical impedance spectra; (f) *J*–*V* curves; (g) external quantum efficiency curves; (h) stability test under continuous light; and (i) *J*–*V* curves after polarization.

radii, implying high charge transfer resistance. This resistance is positively correlated with the parallel resistance of the device, indicating that there are less leakage current and few defects in the active layer, which is beneficial to improving device performance. Under simulated AM 1.5 solar spectrum illumination at 100 mW/cm², the current density–voltage (*J*–*V*) characteristics show a 337% increase in efficiency, with V_{OC} rising to 1.11 V and J_{SC} to 5.17 mA/cm², resulting in a 2.83% power conversion efficiency (Fig. 4(f)). External quantum efficiency testing is employed to characterize the optoelectronic conversion performance (Fig. 4(g)). SCVD-devices exhibited continuous optoelectronic response from 300 to 550 nm, reaching a maximum value of 63.3% at 500 nm, significantly surpassing the 21.8% observed in SC-processed devices. The integrated currents are 1.56 and 5.15 mA/cm², consistent with the *J*–*V* results. Stability testing of the device in Fig. 4(h) indicated the superior stability of SCVD-devices. Under continuous illumination, the SCVD-device remained stable at 85% of the initial efficiency for 100 min, while the SC processing device decayed by 60% within 30 min. The details of V_{OC} and J_{SC} stability results can be found in Fig. S18 in the ESM, SCVD devices demonstrate improved stability. As a ferroelectric photovoltaic device, polarization plays a crucial role in modulating the device's photovoltaic performance (Fig. S19 in the ESM). In the initial state, the dipoles within the polycrystalline molecular ferroelectric film are disordered. photogenerated carriers are separated only by the built-in electric field at the interface between the transport layer and the active layer. After positive polarization, the dipoles within the molecular ferroelectric align, generating a polarization field that is consistent with the direction of the built-in electric field. This polarization field, which extends throughout the material, effectively enhances the separation and transport of photogenerated carriers, thereby improving device performance. After negative polarization, the polarization field against the built-in electric field, inhibiting the transport of photogenerated carriers and degrading device performance. Polarization tests are carried out to characterize the impact of ferroelectricity on device performance (Fig. 4(i)). 1 V polarization can effectively improve device performance, with V_{OC} increasing from 1.11 to 1.25 V, J_{SC} increasing from 5.17 to 7.02 mA/cm², and power conversion efficiency achieving the highest efficiency of 3.8% for two-dimensional (n = 1) Ruddlesden–Popper perovskite solar cells. Although continuing to increase the polarization voltage to

+2 V can slightly increase V_{OC} and J_{SC}, the reduced fill factor limits the further improvement of power conversion efficiency to only 3.62%. The decrease in fill factor may be related to the damage to the film caused by the external electric field during the polarization process. To further confirm the influence of polarization direction on devices performances, negative polarization are performed. As expected, after polarization at −0.5 V, a significant performance degradation occurred, with the most notable reductions in J_{SC} and fill factor, which decreased from 5.17 mA/cm^2 and 49.3% to 3.95 mA/cm^2 and 38.1%, respectively. The final device efficiency degraded to 1.65% (Table S2 in the ESM). The device performance can be effectively modified through ferroelectricity.

3 Conclusion

In summary, this work presents an approach for achieving high-temperature annealing (above decomposition temperature) of molecular ferroelectrics through SCVD. This method suppresses the loss of organic ligands during high-temperature annealing and obtains large-grained molecular ferroelectric films with optimized optoelectronic properties and improved ferroelectricity. The improvements in film quality and optoelectronic properties are significant, characterized by a significant increase in grain size, optimization of band gap, reduced trap-state density, and enhanced carrier mobility. Additionally, the SCVD optimizes the energy level structure of the film to better match the device, leading to improved ferroelectric solar cell performance, indicating the promising development prospects of molecular ferroelectric devices. This work investigates the annealing process of SCVD, providing valuable insights for optimizing high-temperature unstable films and advancing research in ferroelectric devices.

Electronic Supplementary Material: Supplementary material (Experimental section, Figs. S1–S19, Tables S1 and S2, and Video S1) is available in the online version of this article at https://doi.org/10.26599/NR.2025.94907221.

Data availability

All data needed to support the conclusions in the paper are presented in the manuscript and the Electronic Supplementary Material. Additional data related to this paper may be requested from the corresponding author upon request.

Acknowledgements

We gratefully acknowledge the support from the National Natural Science Foundation of China (Nos. 52325309, 22488101, 22405040, and 62005027), the National Key R&D Program of China (No. 2024YFA1509300), GBRCE for Functional Molecular Engineering and Institute of Green Chemistry and Molecular Engineering，the Gusu Innovation and Entrepreneurship Leading Talent Program (No. ZXL2024383), the Key Lab of Advanced Optical Manufacturing Technologies of Jiangsu Province & Key Lab of Modern Optical Technologies of Ministry of Education, and the Natural Science Foundation of Jiangsu Province (No. BK20241267)

Declaration of competing interest

All the contributing authors report no conflict of interests in this work.

Author contribution statement

C. W.: Data curation, project administration, validation, writing manuscript, experimental design. S. C.: Project administration. L. B. X.: Data curation, experimental design. C.-R. H.: Validation. R. N. W.: Writing manuscript. R. J. L.: validation. L. T. L.: Validation. G. F. Z.: Project administration, funding acquistion. Q. Z.: Project administration.

Use of AI statement

None.

References

[1] Chakrabartty, J.; Harnagea, C.; Celikin, M.; Rosei, F.; Nechache, R. Improved photovoltaic performance from inorganic perovskite oxide thin films with mixed crystal phases. *Nat. Photonics* **2018**, *12*, 271–276.

[2] Liu, Y.; Wang, S. F.; Chen, Z. J.; Xiao, L. X. Applications of ferroelectrics in photovoltaic devices. *Sci. China Mater.* **2016**, *59*, 851–866.

[3] Butler, K. T.; Frost, J. M.; Walsh, A. Ferroelectric materials for solar energy conversion: Photoferroics revisited. *Energy Environ. Sci.* **2015**, *8*, 838–848.

[4] Niv, A.; Abrams, Z. R.; Gharghi, M.; Gladden, C.; Zhang, X. Overcoming the bandgap limitation on solar cell materials. *Appl. Phys. Lett.* **2012**, *100*, 083901.

[5] Nakashima, S.; Uchida, T.; Takayama, K.; Fujisawa, H.; Shimizu, M. Influence of the polarization direction of light on the anomalous photovoltaic effect in $BiFeO_3$ thin films. *J. Korean Phys. Soc.* **2015**, *66*, 1389–1393.

[6] Liu, X. T.; Zhang, F. Q.; Long, P. Q.; Lu, T.; Zeng, H. R.; Liu, Y.; Withers, R. L.; Li, Y. X.; Yi, Z. G. Anomalous photovoltaic effect in centrosymmetric ferroelastic $BiVO_4$. *Adv. Mater.* **2018**, *30*, 1801619.

[7] Grinberg, I.; West, D. V.; Torres, M.; Gou, G. Y.; Stein, D. M.; Wu, L. Y.; Chen, G. N.; Gallo, E. M.; Akbashev, A. R.; Davies, P. K. et al. Perovskite oxides for visible-light-absorbing ferroelectric and photovoltaic materials. *Nature* **2013**, *503*, 509–512.

[8] Huang, H. T. Ferroelectric photovoltaics. *Nat. Photonics* **2010**, *4*, 134–135.

[9] Yang, S. Y.; Seidel, J.; Byrnes, S. J.; Shafer, P.; Yang, C. H.; Rossell, M. D.; Yu, P.; Chu, Y. H.; Scott, J. F.; Ager III, J. W. et al. Above-bandgap voltages from ferroelectric photovoltaic devices. *Nat. Nanotechnol.* **2010**, *5*, 143–147.

[10] Bhatnagar, A.; Roy Chaudhuri, A.; Kim, Y. H.; Hesse, D.; Alexe, M. Role of domain walls in the abnormal photovoltaic effect in $BiFeO_3$. *Nat. Commun.* **2013**, *4*, 2835.

[11] Tu, C. S.; Chen, C. S.; Chen, P. Y.; Wei, H. H.; Schmidt, V. H.; Lin, C. Y.; Anthoniappen, J.; Lee, J. M. Enhanced photovoltaic effects in A-site samarium doped $BiFeO_3$ ceramics: The roles of domain structure and electronic state. *J. Eur. Ceram. Soc.* **2016**, *36*, 1149–1157.

[12] Tan, Y. Q.; Zhang, J. L.; Wu, Y. Q.; Wang, C. L.; Koval, V.; Shi, B. G.; Ye, H. T.; McKinnon, R.; Viola, G.; Yan, H. X. Unfolding grain size effects in barium titanate ferroelectric ceramics. *Sci. Rep.* **2015**, *5*, 9953.

[13] Zhang, J. J.; Su, X. D.; Shen, M. R.; Dai, Z. H.; Zhang, L. J.; He, X. Y.; Cheng, W. X.; Cao, M. Y.; Zou, G. F. Enlarging photovoltaic effect: Combination of classic photoelectric and ferroelectric photovoltaic effects. *Sci. Rep.* **2013**, *3*, 2109.

[14] Zhang, H. Y.; Hu, C. L.; Hu, Z. B.; Mao, J. G.; Song, Y.; Xiong, R. G. Narrow band gap observed in a molecular ferroelastic: Ferrocenium tetrachloroferrate. *J. Am. Chem. Soc.* **2020**, *142*, 3240–3245.

[15] Wang, C.; Gu, J. H.; Li, J.; Cai, J. Y.; Li, L. T.; Yao, J. J.; Lu, Z.;

Wang, X. H.; Zou, G. F. Two-dimensional (n = 1) ferroelectric film solar cells. *Natl. Sci. Rev.* **2023**, *10*, nwad061.

[16] Li, H. J.; Liu, Y. L.; Chen, X. G.; Gao, J. X.; Wang, Z. X.; Liao, W. Q. High-temperature dielectric switching and photoluminescence in a corrugated lead bromide layer hybrid perovskite semiconductor. *Inorg. Chem.* **2019**, *58*, 10357–10363.

[17] Ye, H. Y.; Zhou, Q. H.; Niu, X. H.; Liao, W. Q.; Fu, D. W.; Zhang, Y.; You, Y. M.; Wang, J. L.; Chen, Z. N.; Xiong, R. G. High-temperature ferroelectricity and photoluminescence in a hybrid organic–inorganic compound: (3-Pyrrolinium)$MnCl_3$. *J. Am. Chem. Soc.* **2015**, *137*, 13148–13154.

[18] Xiao, L. B.; Xu, X. L.; Lu, Z.; Zhao, J.; Liu, R. Y.; Ye, Y. Q.; Tang, R. J.; Liao, W. Q.; Xiong, R. G.; Zou, G. F. *In-situ* organic–inorganic ferroelectric layer growth for efficient perovskite solar cells with high photovoltage. *Nano Energy* **2023**, *109*, 108114.

[19] Zhang, H. J.; Shi, Z. J.; Hu, L. G.; Tang, Y. Y.; Qin, Z. Y.; Liao, W. Q.; Wang, Z. S.; Qin, J. J.; Li, X. G.; Wang, H. L. et al. Highly efficient 1D/3D ferroelectric perovskite solar cell. *Adv. Funct. Mater.* **2021**, *31*, 2100205.

[20] Xu, X. L.; Xiao, L. B.; Zhao, J.; Pan, B. K.; Li, J.; Liao, W. Q.; Xiong, R. G.; Zou, G. F. Molecular ferroelectrics-driven high-performance perovskite solar cells. *Angew. Chem., Int. Ed.* **2020**, *59*, 19974–19982.

[21] Gu, J. H.; Wang, C.; Xu, X. L.; Xiao, L. B.; Li, J.; Zhao, J.; Zou, G. F. Efficient molecular ferroelectric photovoltaic device with high photocurrent via lewis acid-base adduct approach. *Nanotechnology* **2022**, *33*, 405402.

[22] Wang, J. J.; Zhou, D. Y.; Dong, W.; Yao, Y. F.; Sun, N. N.; Ali, F.; Hou, X. D.; Liu, F. Optimizing annealing process for ferroelectric y-doped HfO_2 thin films by all-inorganic aqueous precursor solution. *Adv. Electron. Mater.* **2021**, *7*, 2000585.

[23] Wang, Y. L.; Damjanovic, D.; Klein, N.; Hollenstein, E.; Setter, N. Compositional Inhomogeneity in Li- and Ta-modified (K, Na)NbO_3 ceramics. *J. Am. Ceram. Soc.* **2007**, *90*, 3485–3489.

[24] Zhang, H. Y.; Song, X. J.; Chen, X. G.; Zhang, Z. X.; You, Y. M.; Tang, Y. Y.; Xiong, R. G. Observation of vortex domains in a two-dimensional lead iodide perovskite ferroelectric. *J. Am. Chem. Soc.* **2020**, *142*, 4925–4931.

[25] Rajendra Kumar, G.; Kim, H. J.; Karupannan, S.; Prabakar, K. Interplay between iodide and tin vacancies in $CsSnI_3$ perovskite solar cells. *J. Phys. Chem. C* **2017**, *121*, 16447–16453.

[26] Quarti, C.; De Angelis, F.; Beljonne, D. Influence of surface termination on the energy level alignment at the $CH_3NH_3PbI_3$ perovskite/C60 interface. *Chem. Mater.* **2017**, *29*, 958–968.

[27] Mirzehmet, A.; Ohtsuka, T.; Abd. Rahman, S. A.; Yuyama, T.; Krüger, P.; Yoshida, H. Surface termination of solution-processed $CH_3NH_3PbI_3$ perovskite film examined using electron spectroscopies. *Adv. Mater.* **2021**, *33*, 2004981.

[28] Wang, C.; Li, L. T.; Xiao, L. B.; Lu, Z.; Wang, R. N.; Xu, Y.; Tang, R. J.; Zhang, Q.; Li, L. Z.; Bai, Z. C. et al. Impact of AlO_X dielectric layer on performance in two-dimensional perovskite photovoltaic devices. *ACS Appl. Energy Mater.* **2023**, *6*, 1208–1217.